Field Response and Surface-Rupture Characteristics of the 2020 M 6.5 Monte Cristo Range Earthquake, Central Walker Lane, Nevada

Rich D. Koehler[*1], Seth Dee[1], Austin Elliott[2], Alexandra Hatem[3], Alexandra Pickering[2], Ian Pierce[4], and Gordon Seitz[5]

Abstract

The *M* 6.5 Monte Cristo Range earthquake that occurred in the central Walker Lane on 15 May 2020 was the largest earthquake in Nevada in 66 yr and resulted in a multidisciplinary scientific field response. The earthquake was the result of left-lateral slip along largely unmapped parts of the Candelaria fault, one of a series of east–northeast-striking faults that comprise the Mina deflection, a major right step in the north–northwest structural grain of the central Walker Lane. We describe the characteristics of the surface rupture and document distinct differences in the style and orientation of fractures produced along the 28 km long rupture zone. Along the western part of the rupture, left-lateral and extensional displacements occurred along northeasterly and north-striking planes that splay off the eastern termination of the mapped Candelaria fault. To the east, extensional and right-lateral displacements occurred along predominantly north-striking planes that project toward well-defined Quaternary and bedrock faults. Although, the largest left-lateral displacement observed was ∼20 cm, the majority of displacements were <5 cm and were distributed across broad zones up to 800 m wide, which are not likely to be preserved in the geologic record. The complex pattern of surface rupture is consistent with a network of faults defined in the shallow subsurface by aftershock seismicity and suggests that slip partitioning between east-striking left-lateral faults and north to northwest-striking right-lateral faults plays an important role in accommodating northwest-directed transtension in the central Walker Lane.

Introduction

The 2020 *M* 6.5 Monte Cristo Range earthquake occurred on 15 May 2020 at 4:03 a.m. local time with epicentral coordinates of 38.169° N, 117.850° W, in a sparsely populated area of western Nevada about 74 km southeast of the town of Hawthorne. The epicentral location was in the easternmost part of the Mina deflection, a tectonic domain within the central Walker Lane characterized by short, subparallel, east- and northeast-striking left-lateral strike-slip and left-oblique normal faults (Stewart, 1988; Wesnousky, 2005a) (Fig. 1). Seismic observations indicate that slip propagated bilaterally along a steeply dipping east–west-striking left-lateral fault for a distance of ∼30 km (Bormann *et al.*, 2020; Ruhl *et al.*, 2020), extending roughly to the Monte Cristo Range in the east and to the Candelaria Hills in the west (Fig. 1). Analyses of near-field geodetic data indicate that the rupture was associated with ∼1 m of left-lateral slip along the fault plane at depth, with a minor component of dip slip (Hammond *et al.*, 2020). Although, the seismic and

geodetic observations are consistent with east–northeast-oriented, left-lateral slip at depth along the eastward projection of the Candelaria fault, the surface ruptures are more complex, occurring along east-, northeast-, and north-trending traces, suggesting complex fault interactions in the shallow crust.

Shaking was widely felt throughout eastern and central California, in Reno and Las Vegas, Nevada, and as far east as Salt Lake City, Utah; however, societal impacts were minor due to the event's remote location. The most significant damage was settlement cracks across U.S. Highway 95 that resulted in temporary closure and required over $2M in repair costs.

1. Nevada Bureau of Mines and Geology, University of Nevada, Reno, Nevada, U.S.A.; 2. U.S. Geological Survey, Moffett Field, California, U.S.A.; 3. U.S. Geological Survey, Golden, Colorado, U.S.A.; 4. Department of Earth Sciences, University of Oxford, Oxford, United Kingdom; 5. California Geological Survey, San Mateo, California, U.S.A.

*Corresponding author: rkoehler@unr.edu
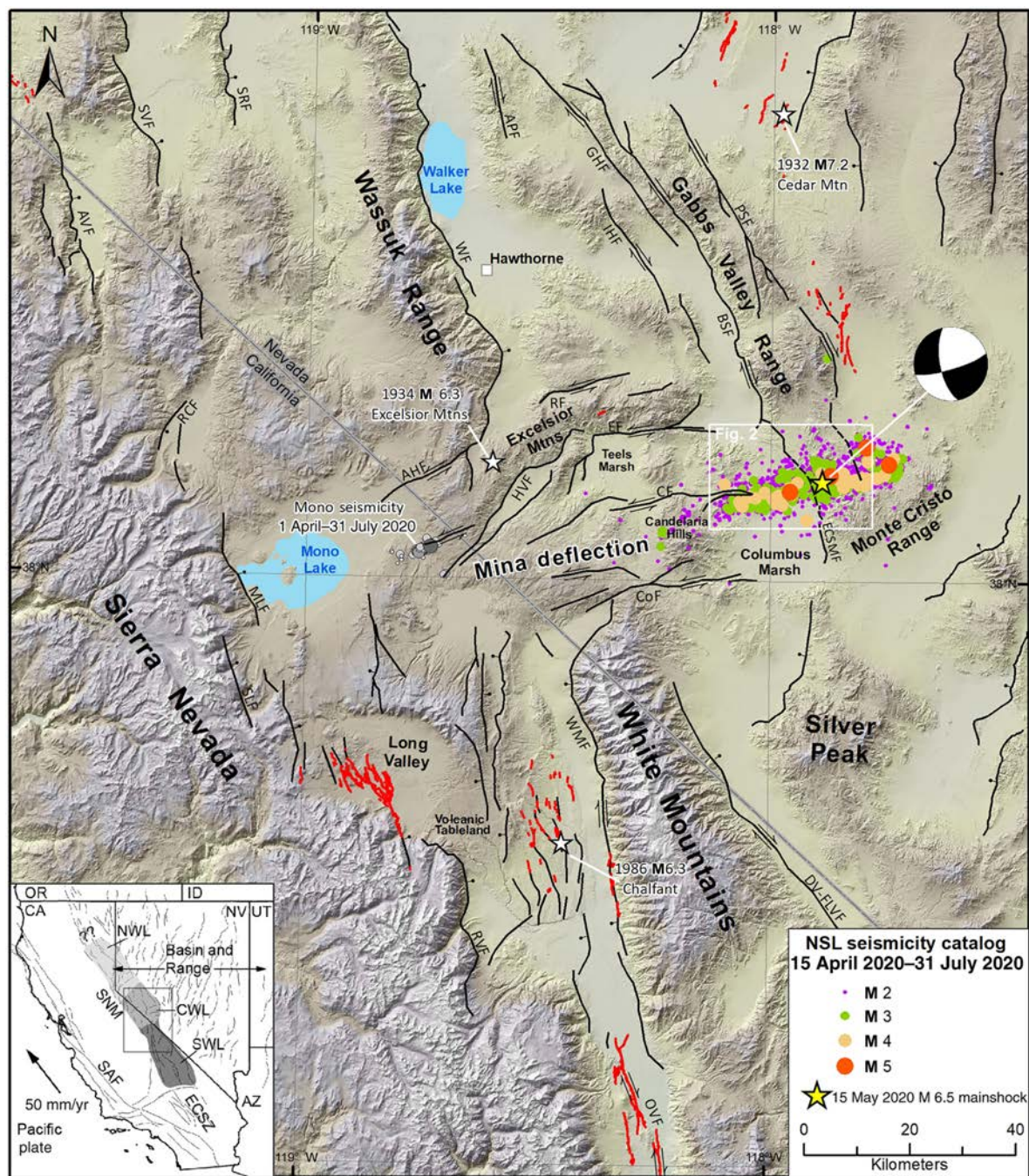
Figure 1. Shaded relief map showing major faults in the region of the 2020 **M** 6.5 Monte Cristo earthquake. Faults modified from Wesnousky (2005a); Faulds and Henry (2008); and Delano *et al.* (2019). The inset map shows tectonic setting of the Walker Lane and Basin and Range in the western United States. The Walker Lane is shown as a shaded belt, including the southern Walker Lane (SWL, dark gray), central Walker Lane (CWL, medium gray), and northern Walker Lane (NWL, light gray). Seismicity data from Nevada Seismological Laboratory (NSL) catalog. SAF, San Andreas fault; SNM, Sierra Nevada microplate; ECSZ, Eastern California shear zone; Focal mechanism from U.S. Geological Survey (USGS). White stars indicate historic earthquake epicenters as labeled, and red lines indicate historic surface ruptures. Major faults of the Mina deflection are Anchorite Hills fault (AHF); Candelaria fault (CF); Coaldale fault (CoF); Excelsior fault (EF); Huntoon Valley fault (HVF); and Rattlesnake fault (RF). Other regional faults (black lines): APF, Agai Pah fault; AVF, Antelope Valley fault; BSF, Benton Springs fault; DV–FLVF, Death Valley–Fish Lake Valley fault system; ECSMF, Eastern Columbus Salt Marsh fault; ECSZ, Eastern California shear zone; GHF, Gumdrop Hills fault; IHF, Indian Head fault; MLF, Mono Lake fault; OVF, Owens Valley fault; PSF, Petrified Springs fault; RCF, Robinson Creek fault; RVF, Round Valley fault; SAF, San Andreas fault; SLF, Silver Lake fault; SMF, Smith Valley fault; SNM, Sierra Nevada microplate; SRF, Singatse Range fault; WF, Wassuk fault; WMF, White Mountain fault. The color version of this figure is available only in the electronic edition.

Despite the relative lack of widespread damage, the event generated considerable interest from earthquake scientists due to (1) its size, the largest magnitude earthquake to occur in Nevada in 66 yr; (2) the lack of previously mapped Quaternary faults at the location of the epicenter; (3) its position between several major historical earthquake ruptures, including the 1872 M_w 7.8–7.9 Owens Valley and 1986 M_w 6.3 Chalfant earthquakes to the south and the 1932 **M** 7.2 Cedar Mountain earthquake to the northeast (Gianella and Callahan, 1934; Beanland and Clark, 1994; Bell *et al.*, 1999; Hough and Hutton, 2008); (4) its relationship to the manner in which geodetically observed strain is accommodated in the central Walker Lane (Wesnousky *et al.*, 2012; Bormann *et al.*, 2016); and (5) the potential for triggered rupture on nearby mapped faults (Barnhart *et al.*, 2020).

Based on the earthquake's magnitude and high probability of surface rupture, a multiagency collaborative effort was initiated the day of the event, to assess the distribution and style of deformation. In this article, we summarize our rapid scientific field response and report on the characteristics of the rupture gleaned through direct field observations. The results provide insight into the complex tectonics of the Mina deflection. The observations have also been compiled into a comprehensive companion rupture distribution map (Dee *et al.*, 2020).

Regional Context

The Monte Cristo Range earthquake surface rupture occurred partly along the Candelaria fault in the central Walker Lane in a region known as the Mina deflection (Fig. 1). The central Walker Lane is part of the larger transtentional Walker Lane system (Stewart, 1988) that extends from the eastern California shear zone to the Modoc plateau along the eastern side of the Sierra Nevada and accommodates ~20%–25% of Pacific North America relative shear (Bennett *et al.*, 1999; Dixon *et al.*, 2000; Hammond and Thatcher, 2007; Lifton *et al.*, 2013). Geologic observations indicate that faults in the southern Walker Lane have an older age of initiation, larger cumulative displacements, and longer more continuous faults, as compared to faults in the central and northern Walker Lane, which become progressively less organized to the north (Faulds *et al.*, 2005; Wesnousky, 2005b). The rate of strain accumulation observed geodetically decreases along the system from about 12 mm/yr in the south to <5 mm/yr in the north and is ~8 mm/yr across the central Walker Lane (Hammond *et al.*, 2011; Bormann, 2013; Bormann *et al.*, 2016).

The Mina deflection is characterized by a series of east- to northeast-striking left-lateral and normal-oblique faults that form a right step between north–northwest-striking right-lateral and right-oblique normal faults to the southwest and northeast (Wetterauer, 1977; Stewart, 1988; DePolo *et al.*, 1993; Oldow *et al.*, 1994; Wesnousky, 2005a; Faulds and Henry, 2008). Quaternary active faults within the Mina deflection include the Rattlesnake, Excelsior, Candelaria, Coaldale,

Anchorite Hills, Huntoon Valley, and eastern Columbus Salt Marsh faults (Fig. 1). Widespread tectonic geomorphic evidence for latest Pleistocene and Holocene left-lateral displacement along the Mina deflection faults was documented by Wesnousky (2005a), including uphill and alternately facing scarps, linear depressions, and deflected drainages, among others. However, a component of extension is indicated by basin-facing scarps across alluvial fan and piedmont surfaces along the ends of some of the faults where they bend to strike north–northeast along range fronts (Wesnousky, 2005a). Post-Pliocene left and left-oblique slip rates have been documented for the Coaldale fault (0.4 mm/yr), Anchorite Hills fault (0.12 mm/yr), and Candelaria fault (0.3 mm/yr), and a post-Pliocene vertical rate across the Excelsior fault has been estimated at 0.01 mm/yr (Gilbert *et al.*, 1968; Speed and Cogbill, 1979; Wesnousky, 2005a; Lee *et al.*, 2006; Tincher and Stockli, 2008).

Southwest of the Mina deflection, right-lateral and right-oblique normal slip is accommodated along a series of north–northwest-striking faults distributed between the Sierra Nevada range front and the White Mountains (Fig. 1). The ~100 km long strike-slip Owens Valley fault accommodates between 1 and 4.5 mm/yr of dextral shear and was the source of the 1872 **M** 7.8–7.9 Owens Valley fault earthquake, which produced lateral displacements up to 6 m (Beanland and Clark, 1994; Lee *et al.*, 2001; Bacon and Pezzopane, 2007; Kirby *et al.*, 2008; Haddon *et al.*, 2016). At its northern end, slip along the Owens Valley fault is partitioned into oblique-normal deformation accommodated along the Round Valley fault (Sierra range front), the White Mountain fault, and a series of faults within the Volcanic Tableland (Nagorsen-Rinke *et al.*, 2013; DeLano *et al.*, 2019). Geologic studies along these faults indicate a vertical slip rate of ~0.4–1 mm/yr across the Round Valley fault (Berry, 1997), 0.5 mm/yr of extension across the Volcanic Tableland (Pinter, 1995), and 0.6 mm/yr and 0.2 mm/yr of right-lateral and extensional deformation, respectively, along the White Mountains fault (Kirby *et al.*, 2006). More recent work along the White Mountains fault indicates that the rate of right-lateral displacement may be as high as 1.4 mm/yr (Lifton *et al.*, 2020). East of the White Mountains, the Fish Lake Valley fault accommodates dextral slip at a late Pleistocene rate of 2.5–6.1 mm/yr (Reheis and Sawyer, 1997; Frankel *et al.*, 2011). Lee *et al.* (2009) and Delano *et al.* (2019) assessed the published slip rates in a kinematic modeling framework, including information from smaller faults in the region, to infer that this fault slip is transferred northward into the southwestern Mina deflection.

Northeast of the Mina deflection, right-lateral shear is accommodated on a series of parallel northwest-striking faults that extend along the east and west sides of the Gabbs Valley Range (Fig. 1). These faults include from west to east the Indian Head, Gumdrop Hills, Benton Springs, and Petrified

Springs faults. Paleoseismic studies along these faults indicate that they each accommodate ~1 mm/yr of dextral slip, representing, approximately, half of the geodetic deformation budget measured for the area (Wesnousky, 2005a; Angster et al., 2019). The 1932 M_w 7.2 Cedar Mountain earthquake occurred to the east of these faults and was associated with strike slip and normal displacements widely distributed along the 75 km length of the rupture (Bell et al., 1999).

Various block models have been proposed to accommodate fault slip across the Mina deflection and are described in detail in Delano et al. (2019). Oldow et al. (1994) suggested that displacement was transferred across the Mina deflection through an extensional stepover defined by normal faults underlain by a low-angle detachment. Wesnousky (2005a, 2020) inferred that the transfer of right-lateral slip across the Mina deflection is accommodated by clockwise rotation of crustal blocks bound by east-striking left-lateral faults. The basins at the ends of the left-lateral faults in the Mina deflection are the result of extensional accommodation adjacent to the rotating blocks. In this model, clockwise rotation of a block bound by the Candelaria fault to the north and Coaldale fault to the south resulted in the formation of the Columbus Marsh basin (Fig. 1). Similarly, block rotations between the Candelaria and Excelsior faults resulted in the development of the Teels Marsh basin. The Wesnousky model is consistent with paleomagnetic data showing 5°–60° of post-Miocene clockwise rotation of crustal blocks in the Mina deflection (Petronis et al., 2009), kinematic models using late-Cenozoic slip rates (Delano et al., 2019), and rotation rates of 1–4°/Ma measured in geodetic block modeling (Bormann et al., 2016).

The Monte Cristo earthquake occurred within a spatial gap between major historical surface rupturing earthquakes to the northeast and south (Fig. 1), the 1932 Cedar Mountain (Bell et al., 1999) and the 1872 Owens Valley events (Beanland and Clark, 1994). Although, seismicity within the Mina deflection is generally diffuse, earthquake clusters with left-lateral focal mechanisms are relatively common, including events in 1980 and 1990 along the Coaldale and Huntoon Valley faults, respectively (Ryall and Priestly, 1975; dePolo et al., 1993). An east–west-striking swarm of small-to-moderate earthquakes occurred just east of Mono Lake, about a month before the Monte Cristo Range earthquake (Fig. 1). The largest earthquake within the Mina deflection—the 1934 M 6.3 Excelsior Mountains earthquake—occurred in the vicinity of the Excelsior fault, approximately, 20 km northwest of the Monte Cristo Range earthquake surface rupture. Field observations after the 1934 event noted, "A break in the surface of the ground along the trace of an old fault extends for, approximately, 4500 feet (1.4 km) across the ridges on the south side of the Excelsior Mountains," (pp. 166) and documented en echelon fissures with opening of up to 8 cm and vertical scarps up to 13 cm high along a 73° north-dipping, 065°-striking fault north of the range front (Callaghan and Gianella, 1935).
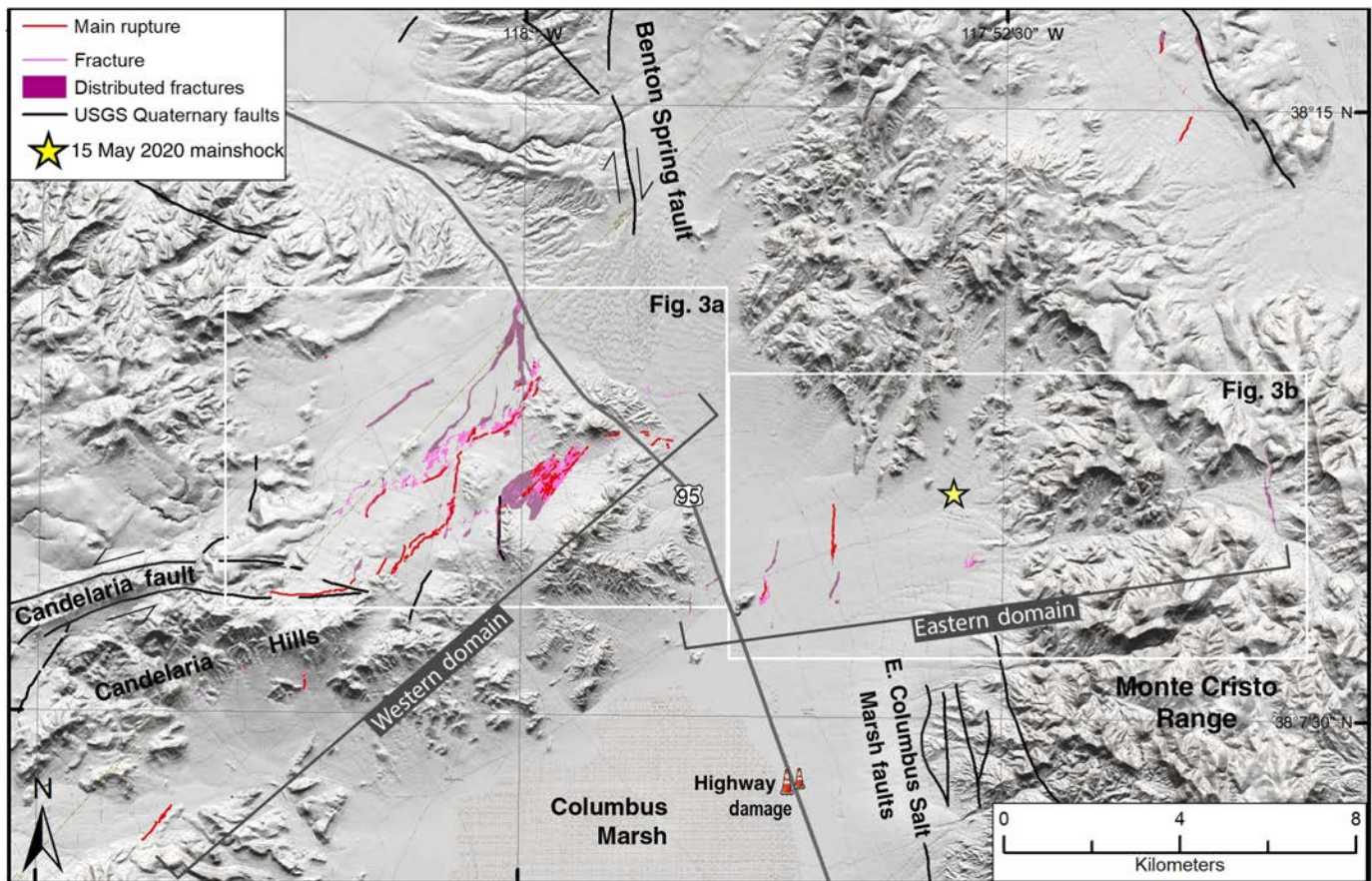
Although, Callaghan and Gianella (1935) did not observe lateral displacements, the en echelon fissures are consistent with left-lateral slip and similar to the Monte Cristo Range earthquake ruptures documented herein.

Earthquake Response

The geologic field assessment team included over 20 scientists from the Nevada Bureau of Mines and Geology (NBMG), California Geological Survey, U.S. Geological Survey (USGS), and several other agencies and consultants. Field surveys were conducted over a two-week period, beginning on the day of the earthquake. Initial observations were communicated to personnel with the Nevada Division of Emergency Management and Homeland Security, Nevada Highway Patrol, Earthquake Engineering Research Institute, and USGS, to evaluate whether or not helicopter support, light detection and ranging data acquisition, and potential launch of a clearinghouse website would benefit the reconnaissance. Based on the limited damage and initial uncertainty of the extent of surface ruptures, these support activities were determined to be unnecessary.

Concurrent with the geologic reconnaissance, the Nevada Seismological Laboratory (NSL) and the Nevada Geodetic Laboratory (NGL) deployed instruments in the vicinity of the earthquake, to monitor ongoing activity including coseismic and postseismic deformation. The NSL installed eight temporary-telemetered seismographs and a local microwave telemetry system. The NGL's MAGNET network had 12 receivers deployed in the epicentral area, at the time of the earthquake, and occupied an additional 24 stations within several weeks. The results of these deployments are discussed in Bormann et al. (2020), Hammond et al. (2020), and Ruhl et al. (2020).

Geologic field mapping was initially focused on the epicentral area east of U.S. Highway 95 the day of the event and progressed to the west over the 10 day investigation. We recorded observations on the location, orientation, continuity, and patterns of surface ruptures, and, where available, the amount and sense of coseismic surface displacement. The relative ages of alluvial fans were qualitatively evaluated using criteria, including surface morphology, dissection, development of dessert varnish, and degree of pavement development (e.g., Bull, 1991). In general, centimeter-scale displacements were preserved in loosely consolidated deposits across alluvial fan surfaces and the subtle margins of ephemeral stream channels, erosional rills, and gullies. Offsets were quantified by tape measurements at over 100 sites, and those offset measurements are presented in Table S1, available in the supplemental material to this article, and archived in Dee et al. (2020). The archived data include location, sense of motion, amount of lateral and vertical displacement, and field notes. The uncertainty in displacement measurements of individual features is shown as a range in Table S1 and on detailed figures. A rainstorm during the field response resulted in overland sheet flow and filling of

Figure 2. Surface-rupture mapping from the **M** 6.5 Monte Cristo earthquake showing mainshock epicenter, the eastern and western rupture domains, location of damage to U.S. Highway 95, and nearby mapped Quaternary faults (black lines; USGS). The color version of this figure is available only in the electronic edition.

centimeter-scale open fractures, highlighting the importance of rapid documentation of fragile geomorphic features associated with surface rupture.

Mapping teams utilized multiple data collection technologies, including handheld and survey grade Global Positioning System (GPS) receivers, as well as various software applications operated on GPS-enabled smartphones and tablets (e.g., ArcCollector, Avenza Maps, and TouchGIS). These technologies have become the standard of practice for rapidly documenting earthquake effects and allow for the colocation of notes, photographs, and locations of observed features. In addition, the ability for field personnel to view multiple linked base maps (satellite imagery, digital elevation models, fault maps, and Interferometric Synthetic Aperture Radar [InSAR] models) and to upload aftershock data in real time on these platforms greatly facilitated the effectiveness and efficiency of the field surveys. Rapidly processed InSAR data provided by the USGS, the Jet Propulsion Laboratory, and other colleagues to field personnel in near-real time proved to be an invaluable resource for guiding the field-mapping effort and locating the most continuous surface ruptures (Elliott *et al.*, 2020).

Low-altitude aerial imagery was collected using uncrewed aerial vehicles (UAVs) (or drones) across areas of the most continuous surface ruptures. Sixteen UAV surveys were performed between 16 May and 7 June 2020, covering a total of 3.7 km² of the rupture. These images were processed with

structure-from-motion photogrammetric software, to develop orthophotomosaics with resolutions ranging from 0.7 to 2.0 cm/pixel. Subsequent to the field effort, the UAV orthoimagery was used to map surface ruptures and fractures at large scales (<1 : 100), complementing field observations and highlighting the complexity of the rupture. A map of the combined field and office observations, including surface ruptures, zones of distributed fracturing, fracture orientations, and the footprints of the orthoimagery, is shown in Figures 2 and 3a,b and presented at more appropriate scales in Dee *et al.* (2020). The full rupture map and associated geospatial data are available for download at the NBMG website (see Data and Resources).

Pattern and Style of Surface Rupture

Distributed surface ruptures were observed across a 28 km long east–northeast-trending zone, extending between the Candelaria Hills in the west and the Monte Cristo Range in the east (Figs. 2
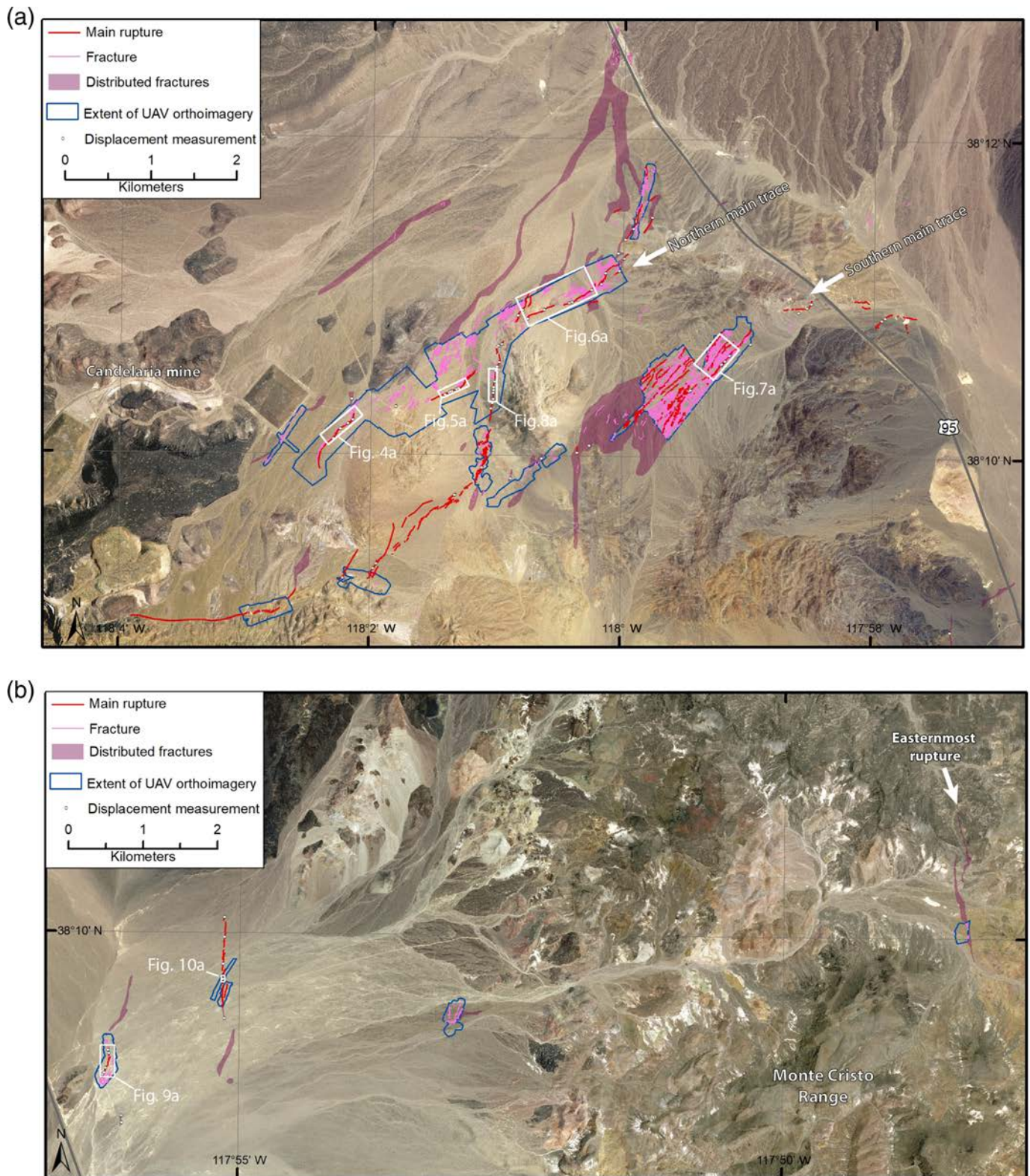
Figure 3. (a) Surface-rupture mapping in the main rupture zone of the western domain showing the north and south main traces. (b) Surface-rupture mapping in the main rupture zone of the eastern domain. Blue lines show the extent of uncrewed aerial vehicle (UAV) orthoimagery and detailed rupture mapping.

Rupture map includes main rupture traces (red lines), traces of fractures (pink lines), zones of distributed fractures in areas without detailed fracture mapping (purple polygons), and locations of displacement measurements. The color version of this figure is available only in the electronic edition.

(a)

(b)

(c)
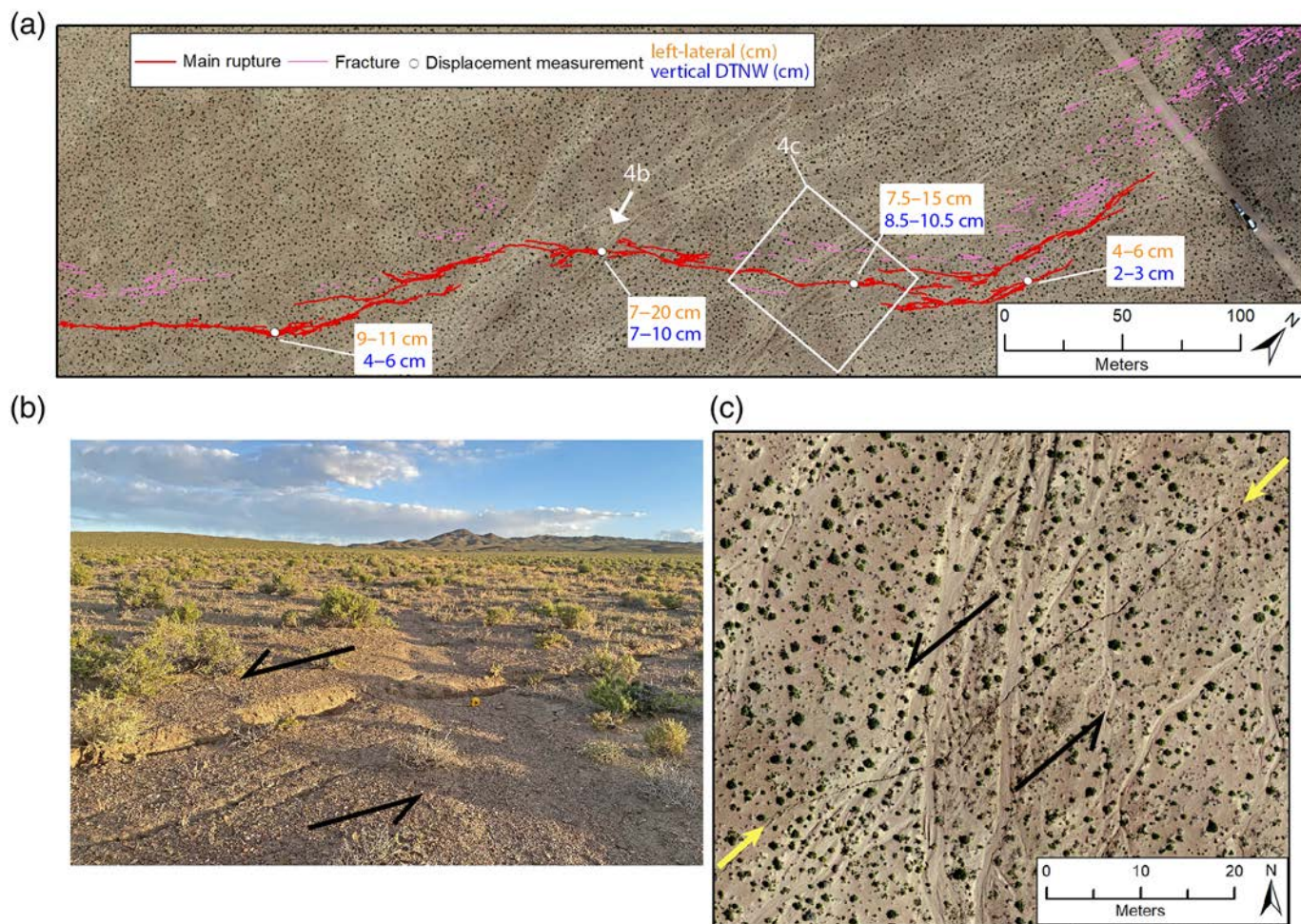
Figure 4. Northern main trace, western rupture domain.
(a) Rupture mapping on UAV orthoimagery showing displacement measurements. (b) Field photo of oblique left-lateral displacement of a channel margin, with 7–20 cm of left lateral and 7–10 cm of down-to-the-northwest vertical displacement (DTNW) measured at this location. (c) UAV orthophoto of a linear and consolidated section of rupture in young alluvial sediment. The color version of this figure is available only in the electronic edition.

and 3). Surface rupture was broadly distributed, with coseismic ground fracturing locally spread across a 2.5–5 km wide area measured perpendicular to the east–west trend delineated by seismicity. Two distinct domains of surface rupture in terms of style and orientation of displacements were observed, roughly separated by U.S. Highway 95, and herein referred to as the eastern and western rupture domains (Fig. 2). In general, ruptures in the eastern domain, near the mainshock epicenter, are predominantly north-striking extensional and right-lateral features that coincide with the projections of north-striking Quaternary and bedrock faults. In contrast, ruptures in the western domain are characterized by left-lateral and extensional displacements along northeasterly and north-striking planes that splay off the eastern termination of the mapped Candelaria fault.

In the following sections, we describe the orientation, style, and distribution of ruptures within each rupture domain and highlight specific features of the ruptures in several key locations (Figs. 4–10).

Western rupture domain

Surface ruptures in the western rupture domain extend, approximately, 10 km from the mapped trace of the Candelaria fault

near the Candelaria Mine (Dohrenwend, 1982; Wesnousky, 2005a) to, approximately, the position of U.S. Highway 95 (Fig. 3a), and measured displacements define east–northeast-striking sinistral and north–northeast-striking extensional faults (Figs. 4–8). The western reach of the ruptures coincides with the east-striking mapped trace of the Candelaria fault for a distance of ∼2 km (Fig. 2), where observable slip dies out westward. To the northeast, distributed ruptures cut across low bedrock hills, pediments, alluvial fans, and active washes. The northeast-ernmost extent of mapped ruptures in the western domain occurs within 3 km of the southernmost mapped trace of the Benton Springs fault (Fig. 2) and consist of distributed cracking.

Although, tectonic geomorphic evidence of progressive Quaternary deformation is present at several places along this zone, Quaternary faults had not previously been mapped along almost all of the surface rupture. Southwest of the Candelaria Hills, several short (<1 km) ruptures were observed; however, no clear connection to the more continuous ruptures to the north was identified (Fig. 2). In addition, field surveys along the Candelaria fault west of the Candelaria Mine, where the fault is well expressed by uphill-facing scarps and laterally displaced drainages, did not find any evidence of coseismic surface rupture.

Along the northwestern flank of the Candelaria Hills, surface ruptures define two subparallel 040°–070°-striking main traces that have a sinuous pattern in map view and are relatively continuous for 9 km (southern trace) and 6 km (northern trace) (Fig. 3a). The two main traces are characterized by complex zones of individual ruptures and fractures. In several locations, these ruptures have overlapping right-stepping en echelon surface breaks, typically 1–15 m long, that are locally connected by 5–10 cm high push-up mounds and mole tracks. Right steps are typically one to several meters across. The geomorphic expression is consistent with left-lateral slip and analogous to the pattern of surface rupture observed in the 2019 **M** 6.4 Ridgecrest California earthquake (Ponti *et al.,* 2020). Left-lateral surface displacements measured along the two main traces range from 1 to 20 cm. Vertical displacements range from 1 to 10 cm along the northern main trace and are consistently down to the northwest. Because of the general lack of clear piercing features, it was difficult to quantify centimeter-scale offsets on many apparent surface ruptures. Subcentimeter displacements were not measured but were commonly observed and sum to centimeter-scale offsets across zones of distributed surface rupture.

Both main rupture traces are associated with wide zones of distributed surface fracturing (pink lines and purple polygons in Fig. 3a), characterized by subparallel and anastomosing closely spaced surface cracks that are open one-to-several centimeters and exhibit both sinuous and sawtooth dilational patterns. The width of distributed fracturing along the southern trace is about 20 m in the west and widens eastward to over 700 m. The northern trace is about 500 m wide in the west and broadens to >2 km wide, because it approaches U.S. Highway 95 to the east.

Details of rupture along the northern main trace are illustrated in detailed rupture maps, orthophotos, and field photographs in Figures 4–6. Figure 4 shows a 040°–045° striking narrowly confined rupture that displaces latest Pleistocene to Holocene alluvial fan deposits. The rupture cuts across a low-gradient piedmont slope, with no pre-existing scarps or adjacent tectonic geomorphology suggestive of previous ruptures. This rupture extends for about 1 km, curves to a more northerly strike at each end, and is partitioned across a highly distributed horsetail geometry to t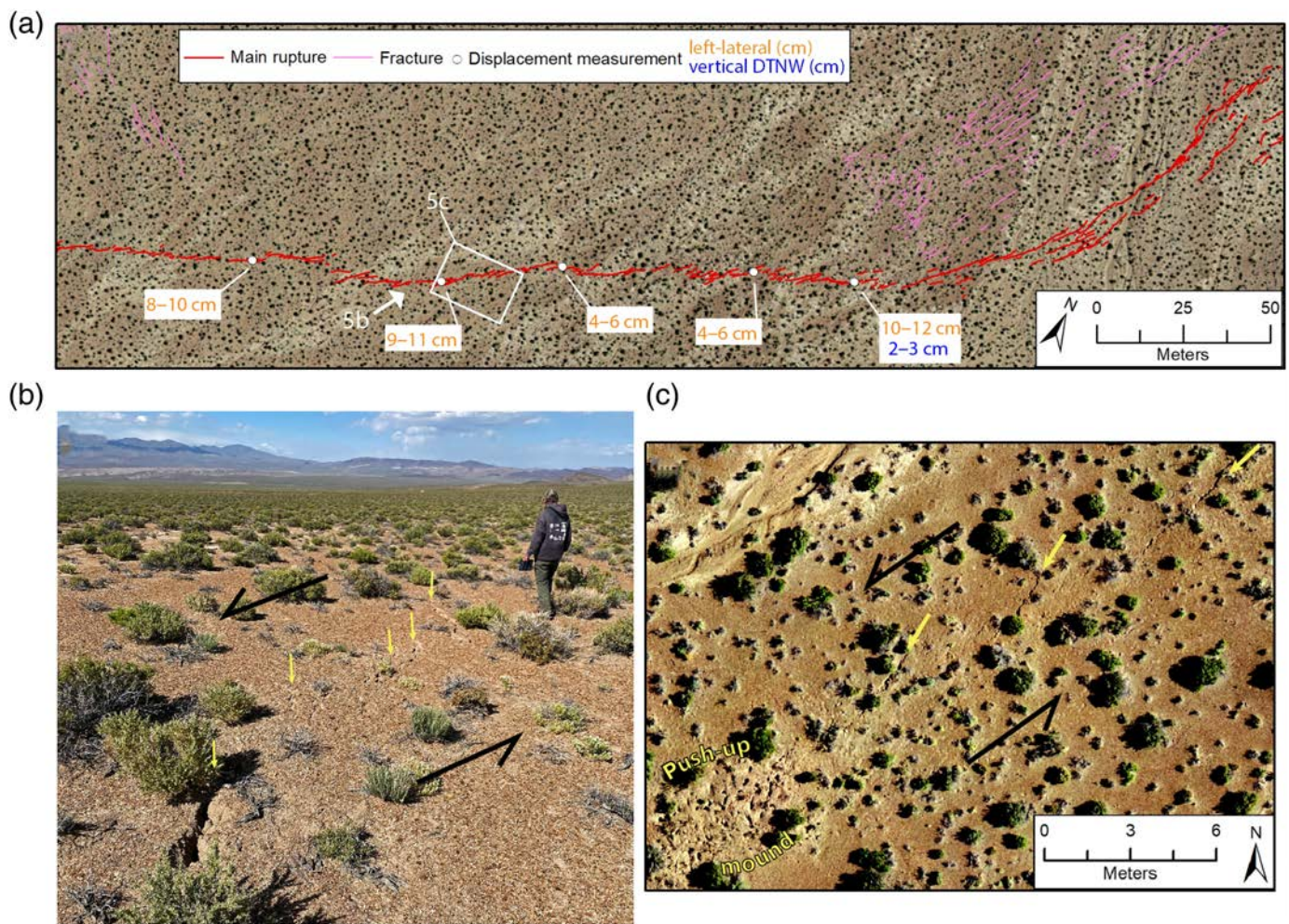he north. The largest left-lateral displacements measured along the entire 2020 surface rupture occur in this area, with a maximum 20 cm left-lateral displacement measured from an offset channel margin and down-to-the-northwest vertical displacements up to 10 cm, showing a component of oblique slip.

One of the more illustrative examples of left-lateral rupture geometry occurs along a 060°–065°-striking rupture shown in Figure 5. The rupture here is characterized by right-stepping en echelon ruptures and mole tracks with little vertical separation. The relatively narrow rupture trace extends for about 700 m across late Pleistocene to Holocene alluvial fan deposits and is not associated with any evidence of prior faulting. The overall orientation of this rupture is similar to the nodal plane of the mainshock but located several kilometers north of the aftershock pattern. This misalignment may partially explain the lack of significant vertical displacement or oblique slip and could indicate triggered shallow slip on this structure.

Observations that document local alignment of surface rupture with previous tectonic deformation are shown in Figure 6. Here, a 025°–030°-striking rupture with left-oblique down-to-the-northwest displacement steps right across a topographically elevated bedrock knob, to a 060°–070°-striking rupture strand with left-oblique down-to-the-southeast displacement. At its crest, the bedrock knob is 2 m higher in elevation than the surrounding alluvial pediment. The alignment of the rupture with the margins of the knob suggests that local uplift within the right step was produced by prior fault rupture(s) at this location. East of the knob, the rupture continues northeast along right-stepping en echelon strands, for about 1 km across a late Pleistocene to Holocene alluvial fan, in which lateral and vertical displacements are up to 17 and 7 cm, respectively. In this area, subparallel extensional fractures are distributed across a 300 m wide zone. An approximate sum of crack opening measurements across the fracture zone north of the main rupture trace in this area indicates, at least, 18 cm of northwest-directed extension.

The southern main trace of the surface rupture is a 9 km long ~050°–060°-striking zone of faulting and fractures, distributed across an area ranging from a few meters to a few hundred meters wide (Fig. 3a). At its western and eastern ends, this zone is defined by relatively narrow, isolated faults that exhibit <5 cm of left-lateral displacement and centimeter-scale opening. In the middle, the southern main trace fault zone widens into an area of exceptionally distributed deformation in alluvial fan deposits (Fig. 3a, area within and adjacent to the white box showing the extent of Fig. 7a). In this area, the rupture is spread over an 800 m wide zone of closely spaced surface breaks. Within the zone of broadest fracturing, the main ruptures can be delineated, based on concentrations and continuity of en echelon ruptures having the largest lateral displacements. These more prominent shear zones, each striking 045°–050°, step successively rightward. An example of the style of the distributed deformation of this area is shown in Figure 7.
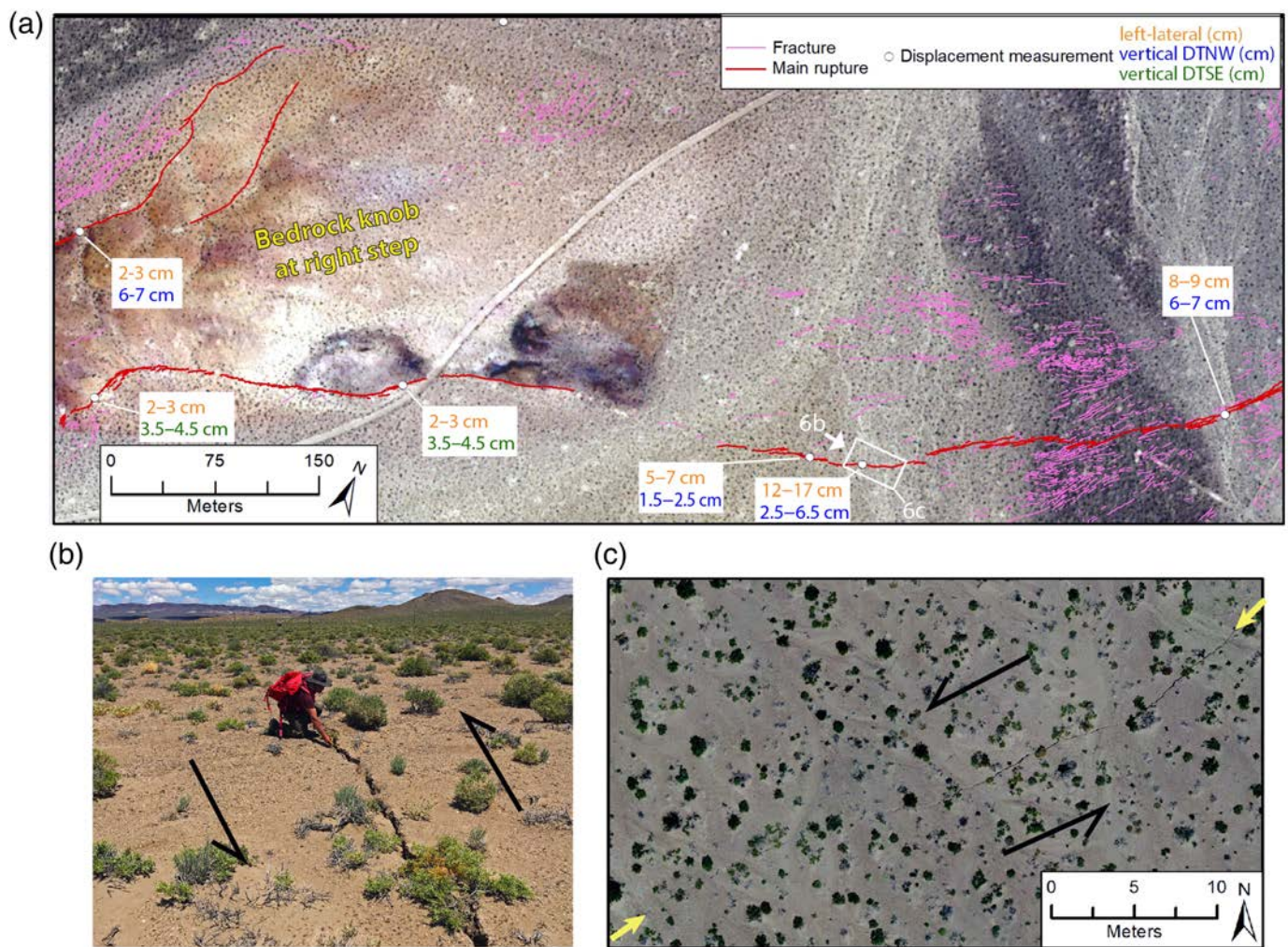
Figure 5. Northern main trace, western rupture domain.
(a) Rupture mapping on UAV orthoimagery showing displacement measurements. (b) Field photo of right-stepping en echelon surface ruptures in left-laterally displaced alluvium. (c) UAV orthophoto of right-stepping en echelon ruptures and a compressional push-up mound. The color version of this figure is available only in the electronic edition.

North–northeast-striking ruptures (005°–030°) splay off both the southern and northern main northeast-striking traces, extend for lengths of 0.5–1.8 km, and are associated with fracture zones between 10 and 100 m wide (Figs. 3a and 8). Individual surface breaks within these ruptures range in length from 5 to 45 m and locally exhibit left-stepping en echelon patterns. Within bedrock, fractures are tight (<1 cm wide); however, in pediment and alluvial fan surfaces, fractures are expressed as 1–5 cm wide extensional openings, with local vertical separations of 1–5 cm. As shown in Figures 3a and 8, the most geomorphically pronounced of these ruptures extends between, and connects, the southern and northern main traces, with an orientation of 005°–010°. This rupture extends across middle and late Pleistocene alluvial fans, and is characterized by down-to-the-west vertical displacement of up to 5 cm and no measurable lateral displacement. Although, we did not observe discernible pre-existing tectonic geomorphic features in Quaternary deposits in this area, the rupture extends along the western base of low bedrock hills that are aligned in a north–south orientation and is coincident with a bedrock fault surface exposed adjacent to the rupture, suggesting prior activity (Fig. 8a).

Eastern rupture domain

Ruptures in the eastern rupture domain are distributed across a 14 km wide area between U.S. Highway 95 and the Monte Cristo Range, and are predominantly north-striking extensional fractures (Figs. 2 and 3b). Two north-striking ruptures extend across the distal piedmont slope in between the Monte Cristo Range and the Candelaria Hills (Figs. 2 and 3b). These ruptures cut late Pleistocene and Holocene alluvial fan and active wash deposits that have smooth profiles and lack geomorphic evidence of previous fault rupture. The westernmost of these ruptures extends continuously at an orientation of 000°–020°, for over 1.5 km (Figs. 3b and 9). Ruptures within this westernmost area are distributed across a 30–40 m wide zone, and are characterized by sinuous overlapping fractures
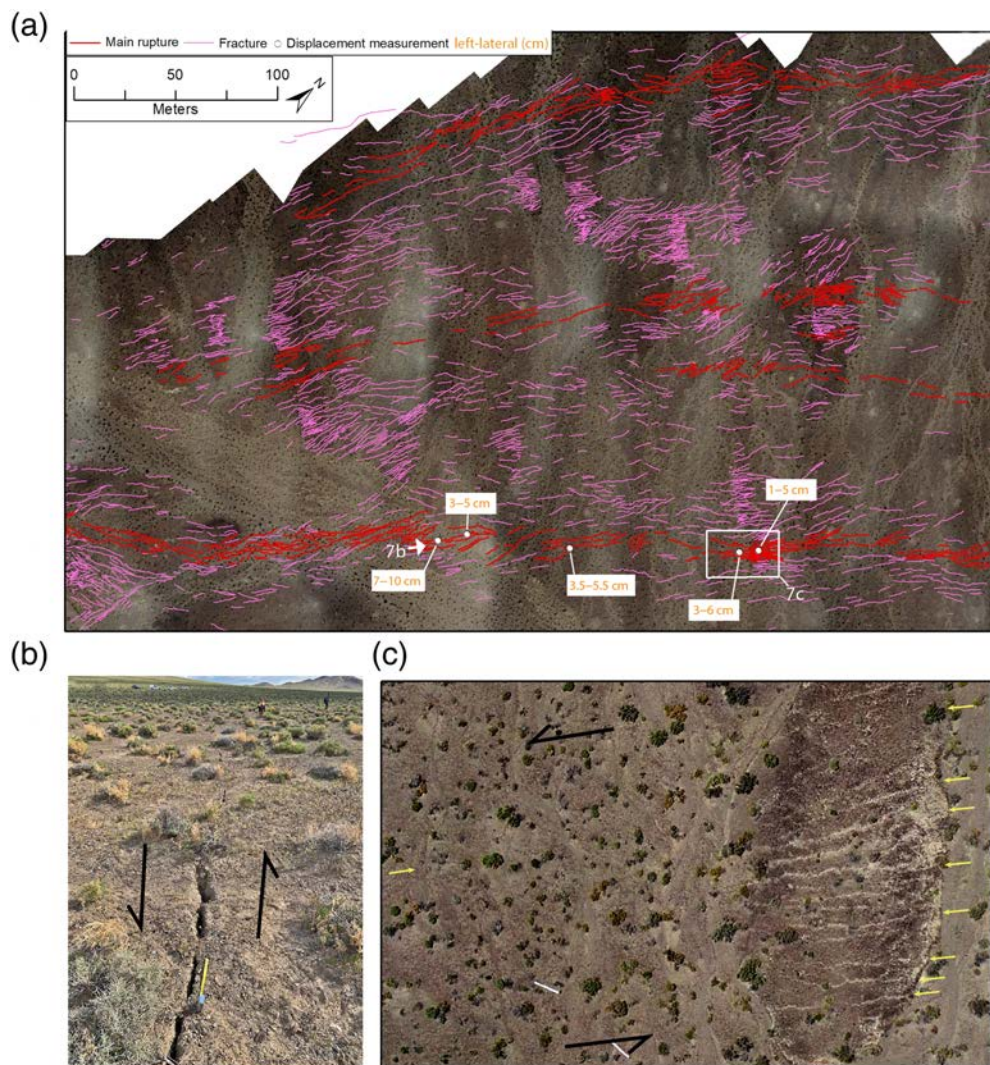
Figure 6. Northern main trace, western rupture domain. (a) Rupture mapping on satellite imagery showing displacement measurements, and the location of a fault-bound bedrock knob at a right step. (b) Field photo of oblique left-lateral displacement of active alluvial channels, with 12–17 cm of left lateral and 2.5–6.5 cm of vertical DTNW measured at this location. (c) UAV orthophoto of a linear section of rupture in young alluvial sediment. Rupture extends between yellow arrows. DTSE, down-to-the-southeast vertical displacement. The color version of this figure is available only in the electronic edition.

with 0.5–3 cm openings and common down-to-the-east and southeast vertical separations of 2–5 cm. Individual fractures are up to 20–45 m long and exhibit an overall left-stepping pattern (Fig. 9a). Another set of similar ruptures occurs 1.5 km to the east and is continuous for over 1.4 km, with an overall orientation of 005° (Figs. 3b and 10). These ruptures have a left-stepping en echelon pattern and right-lateral displacements up to 11 cm, with individual rupture strands ranging in length from 1 to 4 m and striking between 010° and 030°. Both of these ruptures are located between and along the projections of the Benton Springs and Columbus Salt Marsh faults, indicating that they may be associated with a buried north-striking fault that connects those structures at depth (Fig. 2).

At the western range front of the Monte Cristo Range, about 6 km east of U.S. Highway 95, a 600 m wide zone of north–northeast and east–northeast extensional fractures cuts across a relatively old alluvial fan surface, with moderately to well-developed desert pavement (Figs. 2 and 3b). The fractures are predominantly extensional openings of 1–2 cm and oriented 355°–030°. These ruptures extend for, at least, 250 m across the fan surface; however, their extent to the north and south, outside of the limit of the UAV imagery (Fig. 3b), is

unconstrained. A 300 m long rupture oriented orthogonal (70°–100°) to the north-trending fractures is associated with left separations of up to 3 cm and submeter-scale right steps.

The easternmost rupture of the eastern domain strikes, approximately, north–south and is located, approximately, 12.5 km east of U.S. Highway 95 within the Monte Cristo Range. It is continuous for at least 2 km across an alluvial valley and into a linear drainage in bedrock (Figs. 2 and 3b). This rupture coincides with a west-dipping normal fault mapped in bedrock, with tens of meters of down-to-the-west displacement (Stewart *et al.*, 1994). This rupture is characterized by

Figure 7. Southern main trace, western rupture domain. (a) Rupture mapping on UAV orthoimagery and displacement measurements. (b) Field photo of one of the more prominent ruptures. (c) UAV orthophoto of closely spaced fracturing across relatively older alluvial fan surface (yellow arrows). White objects in the orthophoto are overturned mining claim markers. The color version of this figure is available only in the electronic edition.

across a width of 2.5–5 km perpendicular to the east–west trend delineated by seismicity.

In the western domain of the rupture, sinistral-oblique slip along northeast-striking faults and normal right-oblique slip along north–northeast-striking faults splay off the east-striking Candelaria fault and project for about 10 km toward the northwest-striking right-lateral Benton Springs fault (Figs. 2 and 11). The maximum observed left-lateral displacements in the western domain are 20 cm along the northern main traces (Fig. 4) and 10 cm along the southern main traces (Fig. 7), suggesting that the total maximum left-lateral displacement was as much as 30 cm. However, the majority of individual displacement measurements were <5 cm, averaging 4.3–6 cm. Vertical displacements in the western domain were predominantly down to the northwest typically several centimeters (maximum 10.5 cm). In the eastern domain, normal- and right-oblique slips on north-striking faults occurred along strike of the Benton Springs, Petrified Springs, and Eastern Columbus Salt Marsh faults, as well as older mapped bedrock normal faults (Figs. 2 and 11). Displacements there range between 2–5.5 cm (vertical) and 3–5 cm (right-lateral). Appreciable left-lateral surface displacements were not observed along the eastern domain of the rupture.

The distribution of the surface ruptures is generally coincident with the cloud of aftershock seismicity and the location of the geodetically modeled left-lateral slip plane along the eastward projection of the Candelaria fault (Hammond *et al.*, 2020; Ruhl *et al.*, 2020) (Fig. 11). However, the geodetically modeled slip plane, aftershock seismicity, and location of the surface rupture distribution differ in several ways. The western part of the surface rupture has a more northeasterly strike and is several kilometers northwest of the geodetically modeled coseismic slip plane. Hammond *et al.* (2020) suggested that

multiple 350°–360°-striking sinuous and anastomosing fractures distributed across a 40 m wide zone. The fractures are typically open 1–2 cm with occasional down-to-the-west displacements up to 3 cm. This rupture is within a northwest-trending lineament of aftershock seismicity and along the southern projection of the Petrified Springs fault (Figs. 1 and 11).
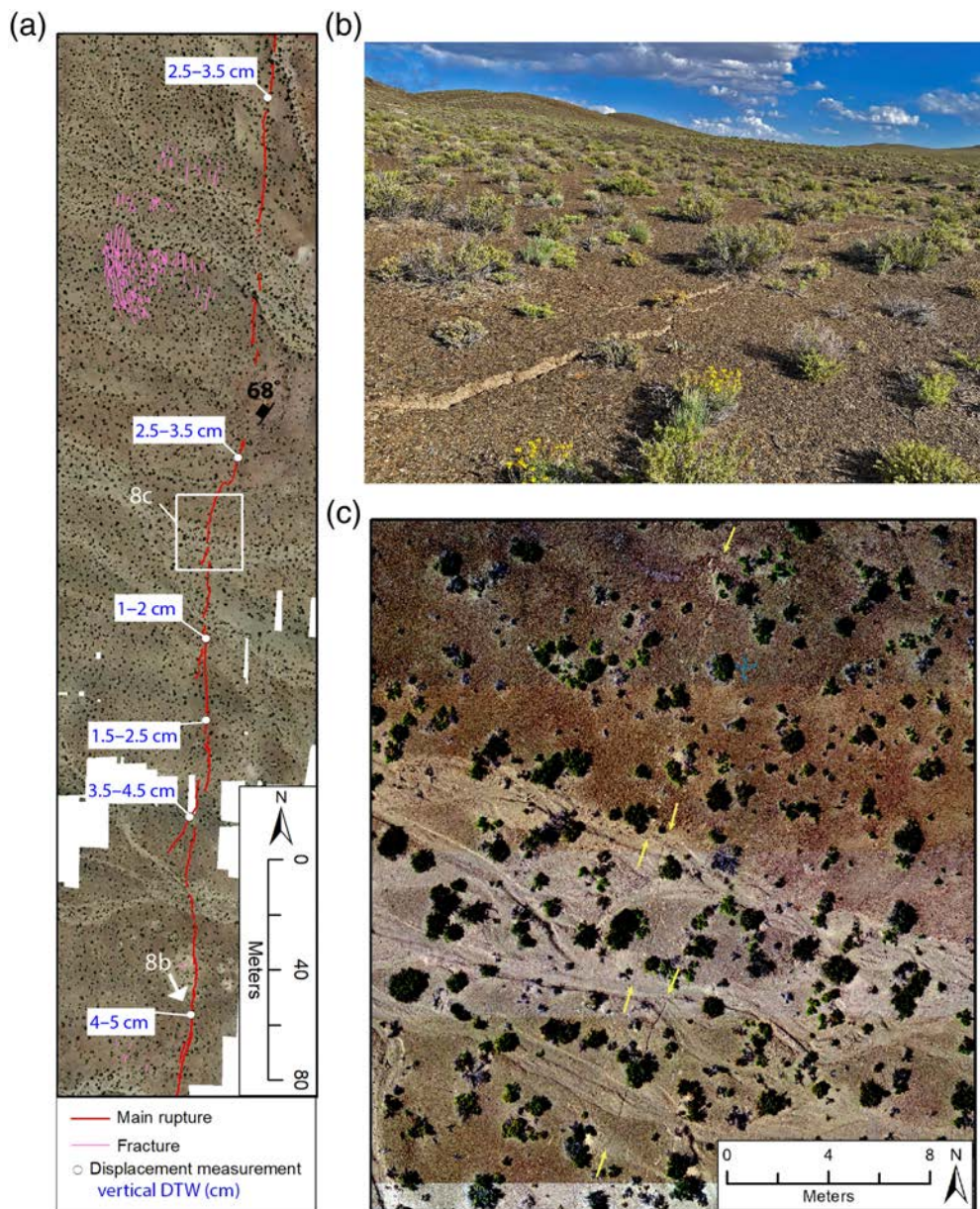
Discussion

The Monte Cristo earthquake surface rupture involved simultaneous rupture and partitioning of slip into sinistral-oblique and dextral-oblique components across a 28 km long network of faults that form a kinematic link between orthogonal regional faults. Coseismic surface faulting was distributed
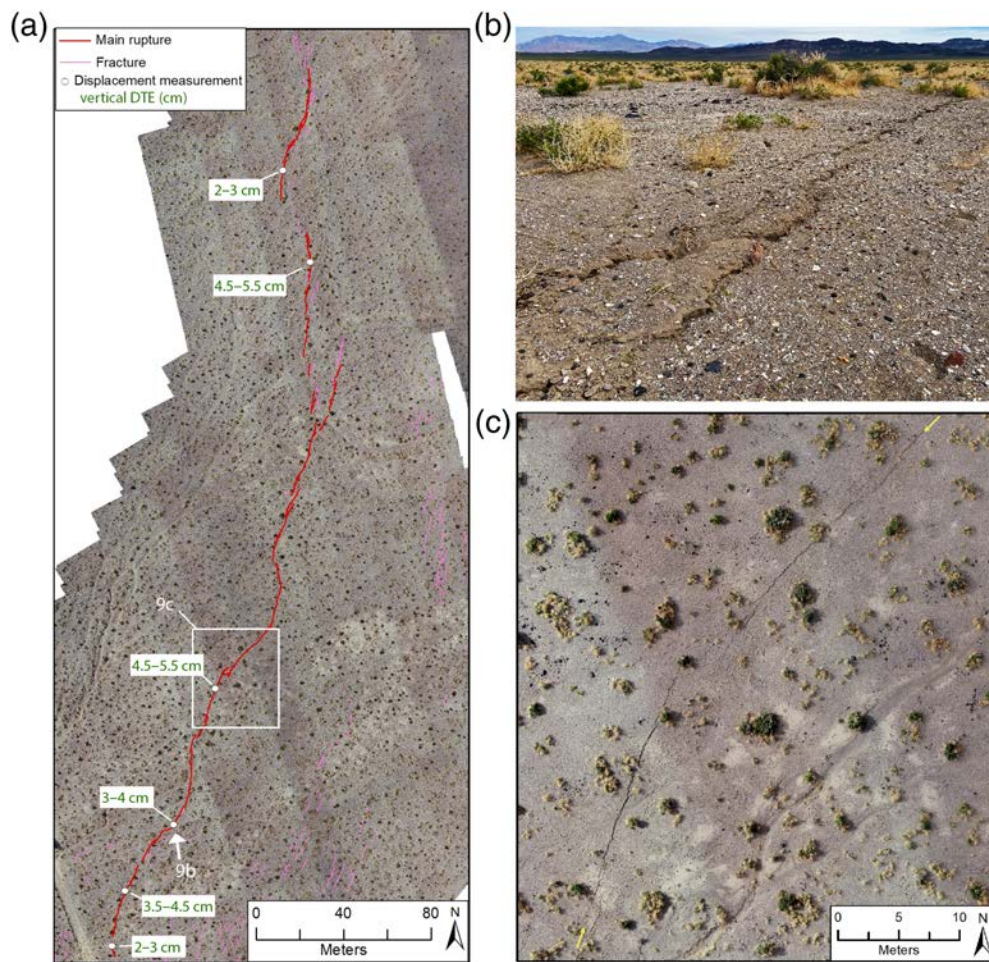
Figure 8. North-striking rupture, western rupture domain. (a) Rupture mapping on UAV orthoimagery showing displacement measurements and the orientation of an exposed bedrock fault surface located on strike with surface rupture (fault surface = 217°/68°). (b) Field photo of vertically displaced (4–5 cm, down-to-the-west [DTW]) alluvium with well-developed desert pavement. (c) UAV orthophoto of rupture cutting variously aged alluvial deposits, including unconsolidated sediment in active channels (lighter colors) and fan gravels with desert pavement (darker colors). The color version of this figure is available only in the electronic edition.

The near-surface rupture complexity in both the eastern and western rupture domains is illustrated by analyses of relocated aftershock seismicity, which defines a network of complex fault geometries in the shallow crust (<6 km) that connect to the primary left-lateral rupture at depth (Ruhl et al., 2020). In the western domain, Ruhl et al. (2020) have shown that the relocated aftershocks define a shallow mesh of faults, with normal and oblique moment tensors along northeast-striking nodal planes. Within this mesh, one prominent zone of seismicity (oriented 065°–070°) projects toward the mapped surface ruptures of the western domain. Ruhl et al. (2020) have also shown that this cluster of seismicity dips to the south, in contrast to the predominantly down-to-the-north observed displacements. In the eastern domain, the seismicity shows even greater complexity, with structures ranging from steeply to moderately dipping and oblique orientations (Ruhl et al., 2020). A north–northwest-striking seismicity lineament, with right-lateral moment tensor nodal planes, closely aligns with a similarly oriented surface rupture having right-lateral displacement (Ruhl et al., 2020) (Figs. 10 and 11). Farther east, alignments of aftershock seismicity are spatially coincident with mapped surface ruptures and project toward the Columbus Salt Marsh and Petrified Springs faults (Fig. 11). The collocation and orientations of the aftershock seismicity lineaments with surface rupture indicate that multiple faults, with variable orientations and kinematics, ruptured simultaneously with the mainshock.

In the central Walker Lane, multiple moderate earthquakes have been associated with complex rupture involving conjugate faults, as summarized in Smith and Priestly (2000) and Ruhl

this location discrepancy may be related to the rupture shallowing and bifurcating in the shallow subsurface at its western end. The eastern rupture domain shows little evidence for slip on an east-striking plane, suggesting that a left-lateral plane in this area is blind. Alternatively, the GPS solution may not accurately resolve the near-surface rupture complexities, possibly due to the analyses being more sensitive to deep slip and the overall body of moment produced by the event.

Figure 9. North-striking rupture, eastern rupture domain. (a) Rupture mapping on UAV orthoimagery showing displacement measurements. (b) Field photo of vertical DTSE (2–5 cm) of Holocene alluvium. (c) UAV orthophoto of a linear section of rupture in Holocene alluvium. DTE, down to-the-east vertical displacement. The color version of this figure is available only in the electronic edition.

et al. (2020). The 1986 M_w 6.3 Chalfant earthquake occurred immediately southwest of the Mina deflection, beneath the Volcanic Tableland adjacent to and immediately west of the White Mountains fault zone (Fig. 1). This earthquake ruptured a northwest-striking right-lateral fault and was preceded by an M_w 5.7 foreshock along a northeast-striking left-lateral fault (Smith and Priestly, 2000). Surface rupture associated with the Chalfant earthquake included centimeter-scale right-oblique and dilational displacements distributed across multiple variably oriented strands (340°–016°) (dePolo and Ramelli, 1987; Lienkaemper *et al.*, 1987). The style and amount of displacement, although, opposite in sense, is similar to the surface ruptures from the Monte Cristo Range and 1934 Excelsior Mountains earthquakes, suggesting that complex, conjugate fault ruptures may be common in the central Walker Lane.

The Mina deflection has not experienced a major **M** 7+ earthquake in historical time, yet sits within a gap in a series of large magnitude events that form a relatively continuous belt extending from the southern Walker Lane to the northern Central Nevada Seismic Belt. These events include, from south to north, the 2019 Ridgecrest, 1872 Owens Valley, 1932 Cedar Mountain, 1954 Dixie Valley, 1954 Fairview Peak, and 1915 Pleasant Valley earthquakes. The historical, moderate-magnitude earthquakes in the region (Chalfant, Monte Cristo Range, and Excelsior Mountains) partially fill the spatial gap; however, they were associated with small displacements and occurred either adjacent to or splaying off of major structures. The physiographic expression and length (15–45 km) of major faults in the Mina deflection, as well as their orthogonal orientation with respect to other major faults, suggest the possibility that future **M** 7+ earthquakes may eventually fill the gap in the belt of major historical seismicity. Alternatively, faults within the Mina deflection are characterized by high-angle bends (25°–45°), connecting strands with strike-slip and normal sense of slip. Biasi and Wesnousky (2017) have shown that these types of complexities can limit the propagation of rupture. Thus, the structural complexities in the Mina deflection may act to limit the length and magnitude of future events.

The style and location of the Monte Cristo Range earthquake surface rupture aligns with current models for deformation in the Mina deflection. In the model of Wesnousky (2005a) for the accommodation of northwest-directed shear, crustal blocks bound by left-lateral east–west-striking faults experience clockwise rotation resulting in basin formation. The absence of a significant basin at the ends of the Candelaria fault led Wesnousky (2005a) to suggest that the total slip on the Candelaria fault is less than neighboring left-lateral faults in the Mina deflection. The lack of strongly expressed geomorphic indications of previous faulting along the Monte Cristo Range earthquake surface rupture is consistent with a weakly developed Candelaria fault. Based on the occurrence of a shallow alluvial basin located immediately northeast of the
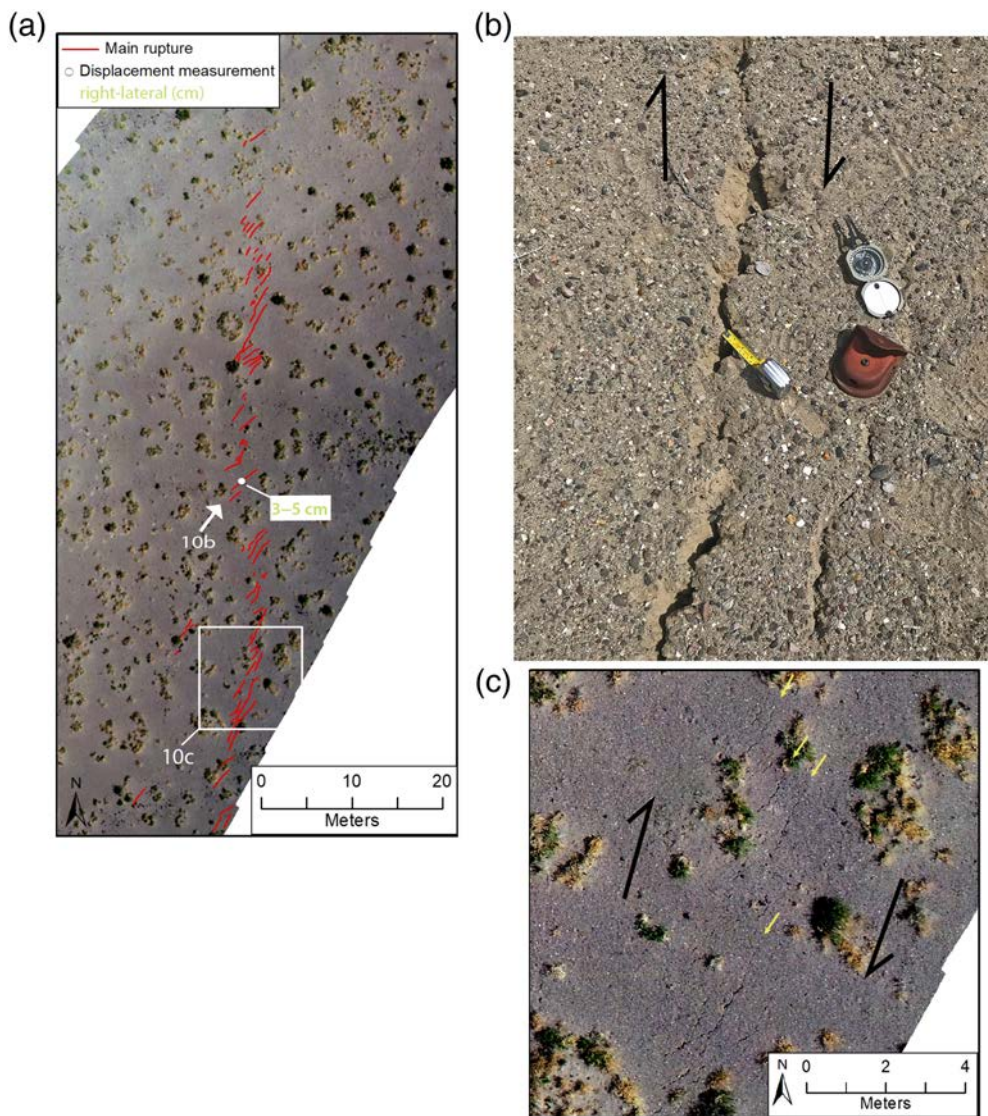
Figure 10. North-striking rupture, eastern rupture domain. (a) Rupture mapping on UAV orthoimagery showing a right-lateral displacement measurement and left-stepping en echelon fractures along a north–northeast-trending rupture. (b) Field photo of 3–5 cm of right-lateral displacement of alluvium, Brunton compass has a north orientation. (c) UAV orthophoto of left-stepping en echelon ruptures that are characteristic of right-lateral slip. The color version of this figure is available only in the electronic edition.

Candelaria fault that is bound on the south by the surface rupture (Figs. 2 and 3a), we hypothesize that the down-to-the-northwest left-oblique displacements observed in this area may have contributed to the development of this immature basin. In this sense, basin development would be consistent with a clockwise rotating block between the Candelaria and Excelsior faults, similar to other basins in the Mina deflection.
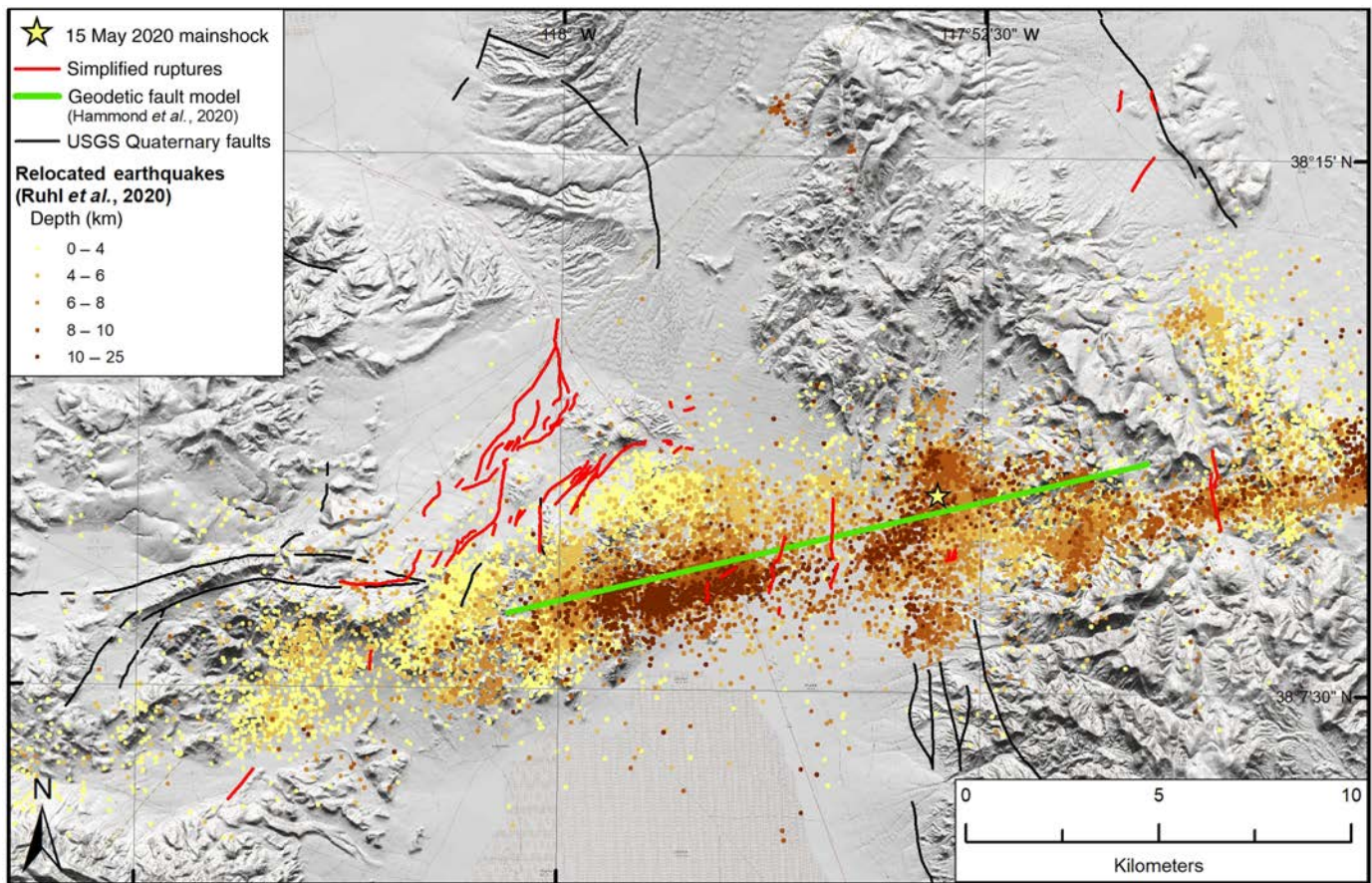
Summary

- The Monte Cristo earthquake was the largest earthquake in Nevada in 66 yr. A multiagency field team immediately

mobilized to the epicentral area, to document the distribution and style of surface rupture. Left-lateral displacements up to 20 cm and right-lateral displacements up to 5 cm occurred along north-east- and north-striking faults, respectively. The surface ruptures were also associated with broad zones of extensional cracking, with individual openings typically 1–3 cm. These small centimeter-scale displacements are unlikely to be preserved in the geologic record and highlight the importance of rapidly documenting these perishable features.

- The earthquake occurred along the eastward projection of the east-striking left-lateral Candelaria fault. However, the surface rupture extended along northeast- and north–northeast-striking faults in areas where Quaternary faults had not been previously mapped. The ruptures project toward the Benton Springs, Petrified Springs, and East Columbus Salt Marsh faults, suggesting that those faults may have been involved in the rupture. The activation of a complex network of faults in the shallow crust is consistent with other historical moderate-magnitude earthquakes in the region.

- The partitioning of slip expressed in the surface rupture and the network of faults defined by the aftershock seismicity are kinematically consistent with the transfer of slip from east-striking left-lateral faults in the Mina deflection to northwest-striking right-lateral faults to the northeast.

- The rupture in the western domain is located north of the aftershock seismicity and suggests fault dips to the north, whereas the seismicity occurs along a south-dipping trend. This discrepancy in the location and sense of displacement between the surface rupture and the aftershock seismicity is difficult to reconcile but may possibly suggest triggered slip in the shallow crust.

Figure 11. Map of simplified surface-rupture traces (red lines) with relocated earthquakes from Ruhl *et al.* (2020) symbolized by depth, the surface trace of the geodetically modeled left-lateral slip plane (green line) from Hammond *et al.* (2020), and mapped Quaternary faults (black lines; USGS). The color version of this figure is available only in the electronic edition.

- It is anticipated that the surface rupture observations will spur additional research questions in this complicated tectonic region. In particular, a comparison of the mapped surface rupture to fringes identified in line-of-sight displacement and InSAR phase gradients would be a fruitful endeavor, to better define the width of rupture and the overall displacement field (Elliott *et al.*, 2020). In addition, the observations will help further evaluate kinematic fault-slip transfer models in the Mina deflection.

Data and Resources

The surface rupture map and associated ArcGIS files referenced in this article are available for download at the Nevada Bureau of Mines and Geology (http://nbmg.unr.edu/Geohazards/Earthquakes/MonteCristo RangeEQData.html, last accessed December 2020). The supplemental material for this article includes information on the location of offset measurements, the amount and sense of displacement, and field notes.

Acknowledgments

References

Angster, S. J., S. G. Wesnousky, P. M. Figueiredo, L. A. Owen, and S. J. Hammer (2019). Late Quaternary slip rates for faults of the central Walker Lane (Nevada, USA): Spatiotemporal strain release in a strike-slip fault system, *Geosphere* **15,** no. 5, 1460–1478.

Bacon, S. N., and S. K. Pezzopane (2007). A 25,000-year record of earthquakes on the Owens Valley fault near Lone Pine, California:

Implications for recurrence intervals, slip rates, and segmentation models, *Geol. Soc. Am. Bull.* **119,** 823–847.

Barnhart, W. D., G. P. Hayes, and R. D. Gold (2020). The July 2019 Ridgecrest California, earthquake sequence: Kinematics of slip and stressing in cross-fault ruptures, *Geophys. Res. Lett.* **46,** 11,859–11,867.

Beanland, S., and M. M. Clark (1994). The Owens Valley fault zone, eastern California, and surface faulting associated with the 1872 earthquake, *U.S. Geol. Surv. Bull. 1982,* 32 pp.

Bell, J. W., C. M. dePolo, A. R. Ramelli, A. M. Sarna-Wojcicki, and C. E. Meyer (1999). Surface faulting and paleoseismic history of the 1932 Cedar Mountain earthquake area, west-central Nevada, and implications for modern tectonics in the Walker Lane, *Geol. Soc. Am. Bull.* **111,** no. 6, 791–807.

Bennett, R. A., J. L. Davis, and B. P. Wernicke (1999). Present-day pattern of Cordilleran deformation in the western United States, *Geology* **27,** no. 4, 371–374.

Berry, M. E. (1997). Geomorphic analysis of late Quaternary faulting on Hilton Creek, Round Valley and Coyote warp faults, east-central Sierra Nevada, California, USA, *Geomorphology* **20,** 177–195.

Biasi, G. P., and S. G. Wesnousky (2017). Bends and ends of surface ruptures, *Bull. Seismol. Soc. Am.* **107,** 2543–2560.

Bormann, J. (2013). New insights into strain accumulation and release in the central and northern Walker Lane, Pacific–North American plate boundary, California and Nevada, USA, *Ph.D. Dissertation,* University of Nevada, Reno, Nevada.

Bormann, J., W. C. Hammond, C. Kreemer, and G. Blewitt (2016). Accommodation of missing shear strain in the central Walker Lane, western North America: Constraints from dense GPS measurements, *Earth Planet. Sci. Lett.* **440,** 169–177.

Bormann, J. M., E. A. Morton, K. D. Smith, G. M. Kent, W. S. Honjas, G. L. Plank, and M. C. Williams (2020). Nevada seismological laboratory rapid seismic monitoring deployment and data availability for the 2020 M 6.5 Monte Cristo Range, Nevada earthquake sequence, *Seismol. Res. Lett.,* doi: 10.1785/0220200344.

Bull, W. B. (1991). *Geomorphic Responses to Climatic Change,* Oxford University Press, Oxford, United Kingdom, 326 pp.

Callaghan, E., and V. P. Gianella (1935). The earthquake of January 30, 1934, at Excelsior Mountains, Nevada, *Bull. Seismol. Soc. Am.* **25,** 161–168.

Dee, S., R. D. Koehler, A. J. Elliott, A. E. Hatem, A. J. Pickering, I. Pierce, G. G. Seitz, C. M. Collett, T. E. Dawson, C. De Masi, *et al.* (2020). Surface rupture map of the 2020 M6.5 Monte Cristo Range earthquake, Esmeralda and Mineral counties, Nevada, *Nevada Bureau of Mines and Geology Map,* scale 1:14,000.

Delano, K., J. Lee, R. Roper, and A. Calvert (2019). Dextral, normal, and sinistral faulting across the eastern California shear zone–Mina deflection transition, California–Nevada, USA, *Geosphere* **15,** no. 4, 1206–1239.

dePolo, C. M., and A. R. Ramelli (1987). Preliminary report on surface fractures alone the White Mountains fault zone associated with the July 1986 Chalfant Valley earthquake sequence, *Bull. Seismol. Soc. Am.* **77,** 290–297.

dePolo, C. M., W. A. Peppin, and P. A. Johnson (1993). Contemporary tectonics, seismicity, and potential earthquake sources in the White Mountains seismic gap, west-central Nevada and east-central California, *Tectonophysics* **225,** 271–299.

Dixon, T. H., M. Miller, F. Farina, H. Wang, and D. Johnson (2000). Present-day motion of the Sierra Nevada block and some tectonic implications for the Basin and Range Province, North America Cordillera, *Tectonics* **19,** no. 1, 1–24.

Dohrenwend, J. C. (1982). Map showing late Cenozoic faults in the Walker Lake 1° by 2° quadrangle, Nevada–California, *U.S. Geol. Surv. Misc. Field Studies Map MF-1382-D,* doi: 10.3133/mf1382D.

Elliott, A. J., S. Dee, R. D. Koehler, W. D. Barnhart, R. Briggs, C. Collett, T. Dawson, S. DeLong, R. D. Gold, E. K. Haddon, *et al.* (2020). Comparison of ground-based and space-based surface rupture mapping of the May 15, 2020 M 6.5 Monte Cristo Range earthquake, Nevada, *Poster number 107 at 2020 SCEC Annual Meeting,* SCEC Contribution number 10489, available at https://www.scec.org/meetings/2020/am/poster/107 (last accessed December 2020).

Faulds, J. E., and C. D. Henry (2008). Tectonic influences on the spatial and temporal evolution of the Walker Lane: An incipient transform fault along the evolving Pacific–North American plate boundary, in *Ores and Orogenesis: Circum-Pacific Tectonics, Geologic Evolution, and Ore Deposits,* J. E. Spencer and S. R. Titley (Editors), Arizona Geological Society Digest 22, 437–470.

Faulds, J. E., C. D. Henry, and N. H. Hinz (2005). Kinematics of the northern Walker Lane: An incipient transform fault along the Pacific–North American plate boundary, *Geology* **33,** 505–508.

Frankel, K. L., J. F. Dolan, L. A. Owen, P. Ganev, and R. C. Finkel (2011). Spatial and temporal constancy of seismic strain release along an evolving segment of the Pacific–North America plate boundary, *Earth Planet. Sci. Lett.* **304,** nos. 3/4, 565–576.

Gianella, V. P., and E. Callahan (1934). The earthquake of December 20, 1932, at Cedar Mountain, Nevada, and its bearing on the genesis of basin range structure, *J. Geol.* **42,** no. 1, 1–22.

Gilbert, C. M., N. M. Christensen, Y. Al-Rawii, and K. R. Lajoie (1968). Structural and volcanic history of Mono basin, California–Nevada, *Geol. Soc. Am. Mem.* **116,** 275–329.

Haddon, E. K., C. B. Amos, O. Zielke, A. S. Jayko, and R. Burgmann (2016). Surface slip during large Owens Valley earthquakes, *Geochem. Geophys. Geosys.* **17,** no. 6, 2239–2269.

Hammond, W. C., and W. Thatcher (2007). Crustal deformation across the Sierra Nevada, northern Walker Lane, Basin and Range transition, western United States measured with GPS, 2000–2004, *J. Geophys. Res.* **112,** doi: 10.1029/2006JB004625.

Hammond, W. C., G. Blewitt, and C. Kreemer (2011). Block modeling of crustal deformation of the northern Walker Lane and Basin and Range from GPS velocities, *J. Geophys. Res.* **116,** doi: 10.1029/2010JB007817.

Hammond, W. C., G. Blewitt, C. Kreemer, R. D. Koehler, and S. Dee (2020). Geodetic observation of seismic cycles before, during, and after the 2020 Monte Cristo Range earthquake using the MAGNET GPS network, *Seismol. Res. Lett.,* doi: 10.1785/0220200338.

Hough, S. E., and K. Hutton (2008). Revisiting the 1872 Owens Valley, California earthquake, *Bull. Seismol. Soc. Am.* **98,** no. 2, 931–949.

Kirby, E., S. Anandakrishnan, F. Phillips, and S. Marrero (2008). Late Pleistocene slip rate along the Owens Valley fault, eastern California, *Geophys. Res. Lett.* **35,** L01304, doi: 10.1029/2007GL031970.

Kirby, E., D. W. Burbank, M. Reheis, and F. Phillips (2006). Temporal variations in slip rate of the White Mountain fault zone, eastern California, *Earth Planet. Sci. Lett.* **248,** 168–185.

Lee, J., J. Garwood, D. F. Stockli, and J. Gosse (2009). Quaternary faulting in Queen Valley, California–Nevada: Implications for kinematics of fault-slip transfer in the eastern California shear zone–Walker Lane belt, *Geol. Soc. Am. Bull.* **121,** nos. 3/4, 599–614.

Lee, J., J. Spencer, and L. Owen (2001). Holocene slip rates along the Owens Valley fault, California: Implications for the recent evolution of the eastern California shear zone, *Geology* **29,** 819–822.

Lee, J., D. Stockli, J. Schroeder, C. Tincher, D. Bradley, L. Owen, J. Gosse, R. Finkel, and J. Garwood (2006). Fault slip transfer in the eastern California shear zone–Walker Lane belt, *Kinematics and Geodynamics of Intraplate Dextral Shear in Eastern California and Western Nevada*, Geological Society of America Penrose Conference Field Trip Guide, Mammoth Lakes, California, 21–26 April, 1–26.

Lienkaemper, J. L., S. K. Pezzopane, M. M. Clark, and M. J. Rymer (1987). Fault fractures formed in association with the 1986 Chalfant Valley, California, earthquake sequence: Preliminary report, *Bull. Seismol. Soc. Am.* **77,** 297–305.

Lifton, Z. M., J. Lee, K. L. Frankel, A. V. Newman, and J. M. Schroeder (2020). Quaternary slip rates on the White Mountains fault zone eastern California: Implications for comparing geologic to geodetic slip rates across the Walker Lane, *Geol. Soc. Am. Bull.* **133,** nos. 1/2, 307–324, doi: 10.1130/B35332.1.

Lifton, Z. M., A. V. Newman, K. L. Frankel, C. W. Johnson, and T. H. Dixon (2013). Insights into distributed plate rates across the Walker Lane from GPS geodesy, *Geophys. Res. Lett.* **40,** 4620–4624.

Nagorsen-Rinke, S., J. Lee, and A. Calvert (2013). Pliocene sinistral slip across the Adobe Hills, eastern California–western Nevada: Kinematics of fault slip transfer across the Mina deflection, *Geosphere* **9,** no. 1, 37–53.

Oldow, J., G. Kohler, and R. A. Donelick (1994). Late Cenozoic extensional transfer in the Walker Lane strike-slip belt, Nevada, *Geology* **22,** 637–640.

Petronis, M. S., J. W. Geissman, J. S. Oldow, and W. C. McIntosh (2009). Late Miocene to Pliocene vertical-axis rotation attending development of the Silver Peak–Lone Mountain displacement transfer zone, west-central Nevada, in *Late Cenozoic Structure and Evolution of the Great Basin-Sierra Nevada Transition*, J. S. Oldow and P. H. Cashman (Editors), Geological Society of America, Special Paper 447, 215–253.

Pinter, N. (1995). Faulting on the volcanic tableland, Owens Valley, California, *J. Geol.* **103,** 73–83.

Ponti, D. J., J. L. Blair, C. M. Rosa, K. Thomas, A. J. Pickering, S. Akciz, S. Angster, J.-P. Avouac, J. Bachhuber, S. Bacon, *et al.* (2020). Documentation of surface fault rupture and ground-deformation features produced by the 4 and 5 July 2019 M_w 6.4 and Mw 7.1 Ridgecrest earthquake sequence, *Seismol. Res. Lett.* 1–18.

Reheis, M. C., and T. L. Sawyer (1997). Late Cenozoic history and slip rates of the Fish Lake Valley, Emigrant Peak, and Deep Springs fault zones, Nevada and California, *Geol. Soc. Am. Bull.* **109,** no. 3, 280–299.

Ruhl, C. J., E. A. Morton, J. M Bormann, R. Hatch-Ibarra, G. Ichinose, and K. Smith (2020). Complex fault geometry of the 2020 M_w 6.5 Monte Cristo Range, Nevada earthquake sequence, *Seismol. Res. Lett.*

Ryall, A. S., and K. Priestly (1975). Seismicity, secular strain, and maximum magnitude in the Excelsoir Mountains area, western Nevada and eastern California, *Geol. Soc. Am. Bull.* **86,** 1585–1592.

Smith, K. D., and K. F. Priestly (2000). Faulting in the 1986 Chalfant, California, sequence: Local tectonics and earthquake source parameters, *Bull. Seismol. Soc. Am.* **90,** no. 4, 813–831.

Speed, R. C., and A. H. Cogbill (1979). Candelaria and other left-oblique faults of the Candelaria region, Nevada, *Geol. Soc. Am. Bull.* **90,** I-149–I-163.

Stewart, J. H. (1988). Tectonics of the Walker Lane belt, western Great Basin: Mesozoic and Cenozoic deformation in a shear zone, in *Metamorphism and Crustal Evolution of the Western United States*, W. G. Ernst (Editor), Prentice-Hall, Englewood Cliffs, New Jersey, 681–713.

Stewart, J. H., P. C. Kelleher, and E. A. Zorich (1994). Geologic map of the Monte Cristo Range area, Esmeralda and Mineral counties, Nevada, *U.S. Geol. Surv. Misc. Field Studies Map MF-2260*.

Tincher, C. R., and D. F. Stockli (2008). Kinematics of multistage Tertiary faulting in the Queen Valley area, central Walker Lane belt, Nevada, in *Late Cenozoic Structure and Evolution of the Great Basin–Sierra Nevada Transition*, J. S. Oldow and P. H. Cashman (Editors), Geological Sociey of America, Special Paper 447, 255–274.

Wesnousky, S. G. (2005a). Active faulting in the Walker Lane, *Tectonics* **24,** TC3009, doi: 10.1029/2004TC001645.

Wesnousky, S. G. (2005b). The San Andreas and Walker Lane fault systems, western North America: Transpression, transtension, cumulative slip, and the structural evolution of a major transform plate boundary, *J. Struct. Geol.* **27,** 1505–1512.

Wesnousky, S. G. (2020). Seismotectonic snapshots: The 18 March M_w 5.7 Magna, 31 March M_w 6.5 Stanley, and 15 May M_w 6.5 Monte Cristo Intermountain West earthquakes of 2020, *Seismol. Res. Lett.*, doi: 10.1785/0220200314.

Wesnousky, S. G., J. M. Bormann, C. Kreemer, W. C. Hammond, and J. N. Brune (2012). Neotectonics, geodesy, and seismic hazard in the northern Walker Lane of western North America: Thirty kilometers of crustal shear and no strike-slip? *Earth Planet. Sci. Lett.* **329/330,** 133–140.

Wetterauer, R. H. (1977). The Mina deflection–A new interpretation based on the history of the Lower Jurassic Dunlap 'formation, western Nevada, *Ph.D. Thesis*, Northwestern University, Evanston, Illinois, 155 pp.